Large Topological Hall Effect and Spiral Magnetic Order in the Weyl Semimetal SmAlSi

Xiaohan Yao[®], ¹ Jonathan Gaudet, ^{2,3} Rahul Verma, ⁴ David E. Graf, ⁵ Hung-Yu Yang, ¹ Faranak Bahrami, ¹ Ruiqi Zhang[®], ⁶ Adam A. Aczel, ⁷ Sujan Subedi[®], ⁸ Darius H. Torchinsky, ⁸ Jianwei Sun, ⁶ Arun Bansil, ⁹ Shin-Ming Huang[®], ¹⁰ Bahadur Singh, ⁴ Peter Blaha[®], ¹¹ Predrag Nikolić[®], ^{12,13} and Fazel Tafti[®], ^{1,*} ¹Department of Physics, Boston College, Chestnut Hill, Massachusetts 02467, USA ²NIST Center for Neutron Research, Gaithersburg, Maryland 20899, USA ³Department of Materials Science and Engineering, University of Maryland, College Park, Maryland 20742-2115, USA ⁴Department of Condensed Matter Physics and Materials Science, Tata Institute of Fundamental Research, Colaba, Mumbai 400005, India ⁵National High Magnetic Field Laboratory, Tallahassee, Florida 32310, USA 6 Department of Physics and Engineering, Tulane University, New Orleans, Louisiana 70118, USA ⁷Neutron Scattering Division, Oak Ridge National Laboratory, Oak Ridge, Tennessee 37831, USA ⁸Department of Physics, Temple University, Philadelphia, Pennsylvania 19122, USA ⁹Department of Physics, Northeastern University, Boston, Massachusetts 02115, USA ¹⁰Department of Physics, National Sun Yat-sen University, Kaohsiung 80424, Taiwan ¹¹Institute of Materials Chemistry, Vienna University of Technology, 1060 Vienna, Austria ¹²Department of Physics and Astronomy, George Mason University, Fairfax, Virginia 22030, USA ¹³Institute for Quantum Matter at Johns Hopkins University, Baltimore, Maryland 21218, USA

(Received 3 June 2022; revised 7 November 2022; accepted 7 February 2023; published 9 March 2023)

Weyl electrons are intensely studied due to novel charge transport phenomena such as chiral anomaly, Fermi arcs, and photogalvanic effect. Recent theoretical works suggest that Weyl electrons can also participate in magnetic interactions, and the Weyl-mediated indirect exchange coupling between local moments is proposed as a new mechanism to induce spiral magnetic ordering by involving chiral Weyl electrons. Here, we present evidence of Weyl-mediated spiral magnetism in SmAlSi from neutron diffraction, transport, and thermodynamic data. We show that the spiral order in SmAlSi results from the nesting between topologically nontrivial Fermi pockets and weak magnetocrystalline anisotropy, unlike related materials (Ce,Pr,Nd)AlSi, where a strong anisotropy prevents the spins from freely rotating. We map the magnetic phase diagram of SmAlSi and reveal an A phase where topological magnetic excitations may exist. Within the A phase, we find a large topological Hall effect whose variation with the magnetic field direction suggests a dominant helical instead of cycloidal character, as theoretically predicted for the Weyl-induced spiral order.

DOI: 10.1103/PhysRevX.13.011035 Subject Areas: Condensed Matter Physics, Magnetism, Materials Science

I. INTRODUCTION

It is well known that the combination of magnetism and topology leads to novel electromagnetic phenomena such as extreme magnetoresistance, quantum anomalous Hall effect, axion insulator, and chiral domain walls [1–7]. It is less known, however, whether topological entities such as Dirac and Weyl fermions can directly participate in

Published by the American Physical Society under the terms of the Creative Commons Attribution 4.0 International license. Further distribution of this work must maintain attribution to the author(s) and the published article's title, journal citation, and DOI.

magnetic interactions and drive specific types of magnetic ordering. Recent calculations show that chiral Weyl electrons could couple to local magnetic moments through the Ruderman-Kittel-Kasuya-Yosida (RKKY) mechanism and mediate indirect Heisenberg $(J_{ij}\mathbf{S}_i \cdot \mathbf{S}_j)$, Kitaev $(K_{\gamma}S_i^{\gamma}S_i^{\gamma})$, and Dzyaloshinskii-Moriya (DM) interactions ($\mathbf{D} \cdot \mathbf{S}_i \times \mathbf{S}_i$) [8–11]. The Weyl-mediated RKKY interactions provide a new mechanism for spiral magnetic ordering and topological magnetic defects (hedgehogs, skyrmions, and meronantimeron pairs) that are in demand for high-density and high-speed memory devices [12–14].

Experimental evidence of such a Weyl-mediated RKKY interaction has recently been found in NdAlSi, a Weyl semimetal with an incommensurate modulated spin density wave (SDW) whose wavelength is linked to the nesting

fazel.tafti@bc.edu

vector between certain pairs of topologically nontrivial Fermi pockets [15]. However, a strong magnetocrystalline anisotropy (MCA) in NdAlSi prevents the spins from rotating freely and establishing a spiral order promoted by the Weyl electrons. Instead, NdAlSi shows a ferrimagnetic order, and the only indication of the Weyl electrons' chirality in its magnetism is a slight canting of spins with a period that matches the distance between the Weyl nodes [15]. Finding the anticipated spiral order and other aspects of chiral magnetism mediated by Weyl electrons remains an open problem.

In this work, we provide multiple experimental evidence of a spiral order in SmAlSi. Using neutron diffraction, we show that the observed ordering wave vector can be described as cycloidal or helical or a mixed spiral structure. We map the phase diagram of SmAlSi using magnetization and heat capacity data and find an A phase featuring topological Hall effect (THE) similar to that seen in helimagnets such as MnSi and Gd₃Ru₄Al₁₂, where skyrmions are found [16,17]. Our band-structure calculations indicate that these manifestations of chiral magnetism can be produced only by Weyl electrons in SmAlSi, which has a vanishing density of states and chiral Fermi pockets that are separated in momentum space by the spiral ordering wave vector. We also experimentally reveal an imprint of Weyl electrons' chirality on the magnetism of SmAlSi by measuring the anisotropy of THE, which can be explained by a spiral order with a dominant helical character, as expected from Weyl-induced RKKY interactions and opposite to the cycloidal character expected from conventional DM interactions.

II. METHODS

Single crystals of SmAlSi are grown using a self-flux method [18]. A Bruker D8 ECO system is used for powder x-ray diffraction, and the FullProf suite is used for the Rietveld refinement [19]. The electrical transport, heat capacity, and magnetic susceptibility are measured using the Quantum Design PPMS Dynacool and MPMS-3 instruments. A piezoresistive technique is used for magnetometry at the National High Magnetic Field Laboratory.

The neutron diffraction experiment is performed with the fixed-incident-energy (14.5 meV) neutron triple-axis spectrometer HB-1A in the High Flux Isotope Reactor (HFIR) at the Oak Ridge National Laboratory, and the SARAh software is used for the representational analysis of the magnetic structure [20]. It is challenging to detect magnetic Bragg peaks in a naturally abundant $^{149}\mathrm{Sm}^{3+}$ crystal, because it has a large neutron absorption cross section ($\sigma_{abs}=42\,080$ b) and a small moment (0.7 μ_B). Using $^{154}\mathrm{Sm}$ ($\sigma_{abs}=8.4$ b) could help, but this isotope is available only in oxide form, not suitable for growing SmAlSi crystals. Thus, we take advantage of the recent monochromator upgrade of the HB-1A spectrometer, which leads to a 3.5 increase of the incident neutron flux.

Density functional theory (DFT) calculations with the full-potential linearized augmented plane-wave method are implemented in the WIEN2K code [21] using the Perdew-Burke-Ernzerhof exchange-correlation functional [22], spin-orbit coupling (SOC), and on-site Coulomb repulsion (Hubbard U) [23]. Monte Carlo simulations are performed using the Metropolis algorithm.

III. RESULTS AND DISCUSSION

A. Heat capacity

SmAlSi belongs to a family of RAlSi Weyl semimetals that have magnetic rare-earth (R^{3+}) ions in a noncentrosymmetric space group $I4_1md$ (inset in Fig. 1 and Fig. S1 [24]) [24–27]. The key parameter that enables spiral ordering in SmAlSi, unlike in other RAlSi compounds, is a weak MCA that allows the spins to rotate freely. The MCA can be quantified using the heat capacity and magnetic susceptibility data. We isolate the magnetic heat capacity (C_m) of RAlSi in Fig. 1 by subtracting the phonon background using the nonmagnetic isostructural compound LaAlSi (Fig. S2 [24]).

The broad Schottky anomaly at T_{CEF} in Figs. 1(a)–1(c) is due to crystal electric field (CEF) excitations, and the sharp peaks at T_1 and T_2 are due to magnetic ordering. We model the Schottky anomaly by assuming a doublet ground state separated from excited multiplets in the Kramers ions Ce³⁺, Nd³⁺, and Sm³⁺ (Fig. S2) [24]. Our Schottky fits [black

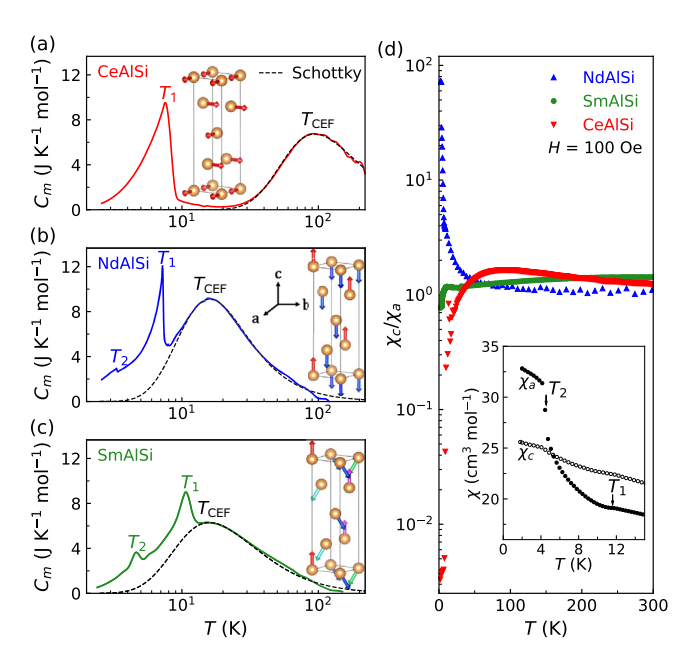


FIG. 1. Magnetic heat capacity is plotted as a function of the temperature in (a) CeAlSi, (b) NdAlSi, and (c) SmAlSi. The broad Schottky anomaly is due to crystal field levels, and the sharp peaks are magnetic transitions. The insets illustrate in-plane magnetic order in CeAlSi, out-of-plane order in NdAlSi, and spiral order in SmAlSi, consistent with the χ_c/χ_a ratios in (d), where CeAlSi and NdAlSi show strong in-plane and out-of-plane anisotropy, but SmAlSi shows χ_c/χ_a of the order of one.

TABLE I. T_{CEF} and Δ are extracted from the Schottky fits in Fig. 1 (see Fig. S2 [24]). The softening of MCA is reflected in the systematic reduction of T_{CEF} , Δ , and the χ_c/χ_a ratio at 2 K. The PrAISi data are reproduced from Ref. [25].

Material	T_{CEF} (K)	$\Delta \ (meV)$	T_1 (K)	T_2 (K)	χ_c/χ_a
CeAlSi	91(7)	29(11)	8.2(2)		$(188)^{-1}$
PrAlSi	30(6)	18(9)	17.8(2)		194
NdAlSi	16(3)	6(2)	7.2(1)	3.3(1)	84
SmAlSi	15(3)	5(2)	10.6(2)	4.6(2)	0.8

dashed lines in Figs. 1(a)–1(c)] yield CEF gaps $\Delta=29(11)$, 6(2), and 5(2) meV in CeAlSi, NdAlSi, and SmAlSi, respectively. The systematic reduction of Δ and T_{CEF} in Table I shows a general softening of the MCA from R= Ce to Nd and Sm. This is also reflected in the systematic change of the ratio between out-of-plane and in-plane magnetic susceptibility χ_c/χ_a at 2 K. As shown in Fig. 1(d) and Table I, CeAlSi has an easy plane with $\chi_c/\chi_a\approx 1/200$, and NdAlSi has an easy axis with $\chi_c/\chi_a\approx 80$. In contrast, SmAlSi has a negligible MCA with $\chi_c/\chi_a\approx 1$ [inset in Fig. 1(d)], which allows the spins to rotate in a spiral order.

B. Neutron diffraction

We align a single crystal of SmAlSi within the (*HHL*) plane and probe the Bragg peaks along the high-symmetry

directions of a few Brillouin zone (BZ) centers. The intensity of the nuclear Bragg peaks does not increase below T_1 or T_2 , ruling out a $\mathbf{k}=(0,0,0)$ ferromagnetic (FM) order. Instead, we find antiferromagnetic (AFM) Bragg peaks at $\mathbf{Q}=(\frac{1}{3}-\delta,\frac{1}{3}-\delta,4)$ and $(\frac{1}{3}-\delta,\frac{1}{3}-\delta,8)$, which can be indexed by an incommensurate vector $\mathbf{k}=(\frac{1}{3}-\delta,\frac{1}{3}-\delta,0)$ with $\delta=0.007(7)$ [Fig. 2(a)]. The temperature dependence of the AFM peak intensity in the inset in Fig. 2(a) shows the onset of the order parameter at $T_1=10.6(2)$ K.

The magnetic ordering vector $\mathbf{k} = (\frac{1}{3} - \delta, \frac{1}{3} - \delta, 0)$ in SmAlSi is similar to the incommensurate ordering vector observed in NdAlSi [15] and indicates an SDW propagating along the [1, 1, 0] direction [Figs. 2(b) and 2(c)]. However, the large Ising MCA in NdAlSi prevents spiral ordering and drives a ferrimagnetic up-down-down order with a net FM component [15], whereas the weak MCA for fixed-magnitude moments in SmAlSi requires the magnetic order with no FM component at the observed wave vector \mathbf{k} to be spiral.

By performing a magnetic representation analysis [20], we identify six possible spin structures that yield a $\mathbf{k} = (\frac{1}{3} - \delta, \frac{1}{3} - \delta, 0)$ vector in SmAlSi and have constant magnetization on each Sm site. We plot the six possible spin structures in Fig. 2(d), assuming $\delta = 0$ (ideal 120° order) for a simple visualization. Their magnetic unit cell is

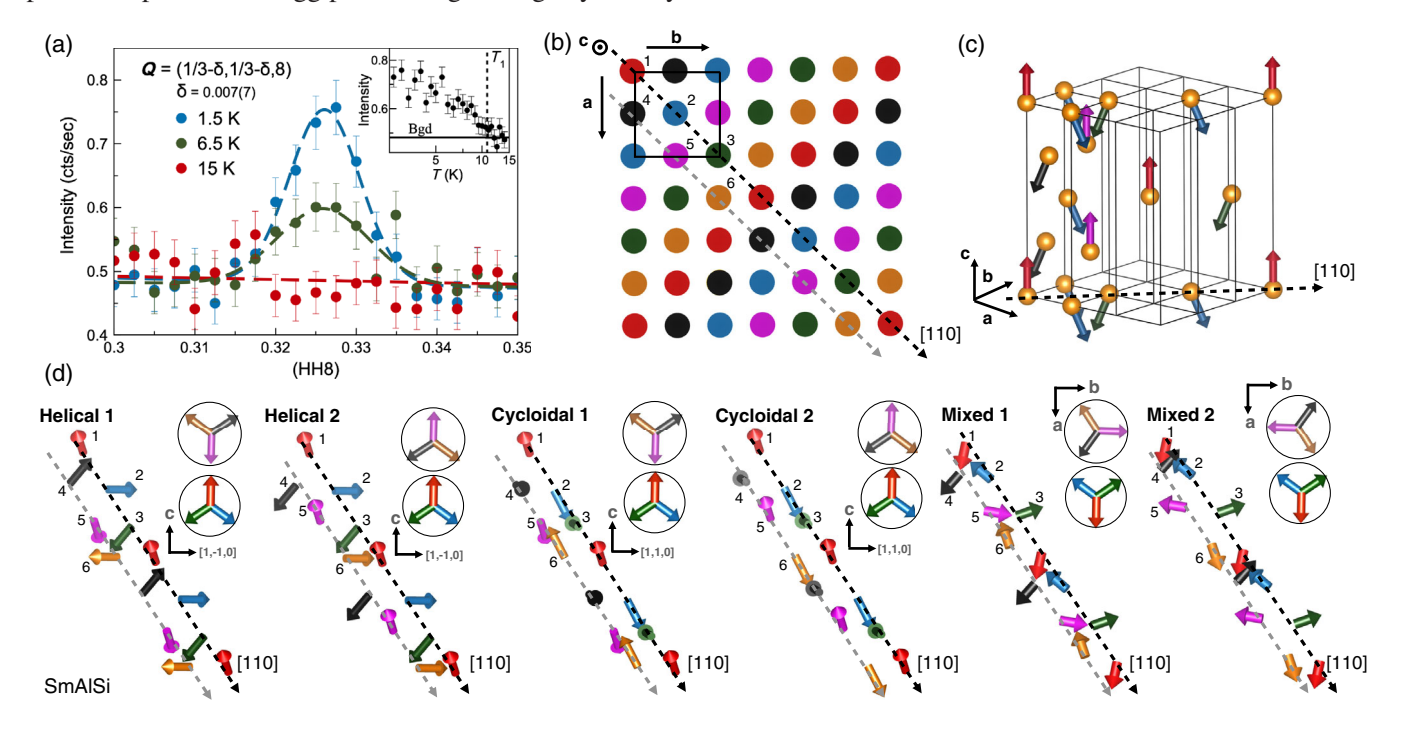


FIG. 2. (a) Neutron diffraction scan along the (HH8) direction in SmAlSi, which reveals a temperature-dependent Bragg peak at $\mathbf{Q} = (\frac{1}{3} - \delta, \frac{1}{3} - \delta, 8)$. The top right inset is the temperature dependence of the Bragg peak intensity. Error bars correspond to one standard deviation. (b) View of the magnetic unit cell for a $\mathbf{k} = (\frac{1}{3}, \frac{1}{3}, 0)$ ordering vector. Each color represents a different spin orientation on a particular Sm site. The black box represents the size of the structural unit cell. (c) 3D rendition of one possible spin structure. (d) Sketches of all six possible spiral orders in SmAlSi. The different colors represent different spin orientations as in (b).

 $3 \times 3 \times 1$ times the structural unit cell and contains up to six different spins in an *ABC*-type structure propagating among both the (0, 0, 0) and $(0, \frac{1}{2}, \frac{1}{4})$ Sm sites as shown in 2D and 3D, respectively, in Figs. 2(b) and 2(c).

All six structures in Fig. 2(d) are spiral but with different chirality. First, there is a helical order where the spins are constrained in the plane perpendicular to the [1, 1, 0] propagation vector. Second, there is a cycloidal order where the spins are constrained in the plane parallel to the [1, 1, 0]propagation vector. Finally, there is a mixed spiral order where the spins are constrained within the basal plane so they have a component that oscillates both perpendicular and parallel to the propagation vector. There are two copies of each type of spiral with in-phase and antiphase ordering between the (0, 0, 0) and $(0, \frac{1}{2}, \frac{1}{4})$ Sm sites. Of these six possible configurations, the first two (helicals 1 and 2) are consistent with the theoretical prediction that the D vector in the Weyl-induced *extended-range* DM interaction tends to be parallel to the direction between the interacting spins wherever the lattice symmetry allows [9]. If a conventional DM interaction is responsible for the spiral order, the **D** vectors must be perpendicular to the nearest-neighbor bonds in the ab layers of the crystal due to the mirror planes in the tetragonal structure of SmAlSi, and the cycloidal spirals would be preferred. As discussed below, we use the angle dependence of THE to distinguish between these two scenarios.

C. Magnetization

In the idealized drawings in Fig. 2(d), the spins rotate 120° with respect to each other, such that no net magnetization is produced over an ABC cycle. For SmAlSi, however, the spins rotate with 120.2(2)° with respect to each other due to the possible small incommensurability (δ) , which would produce a magnetic unit cell size of about 263 nm long with no net magnetization. This is consistent with our M(H) curves in Figs. 3(a) and 3(b) that show the absence of hysteresis near zero field for both H||a| and H||c. At finite fields, however, we observe hysteretic metamagnetic transitions when H||a| [Fig. 3(a)] but not when H||c| [Fig. 3(b)]. The magnitude of M(H = 7 T) is only $0.045\mu_B$, which is an order of magnitude less than the expected value for Sm³⁺ $(0.7\mu_B)$. The hysteretic metamagnetic transitions with small amplitudes for H||a|and the strictly linear M(H) curves when H||c| are characteristics of materials with topological skyrmion excitations, e.g., $GaV_4(S, Se)_8$ and Gd_2PdSi_3 [28–31].

We construct a magnetic phase diagram for SmAlSi based on two sets of peaks in dM/dH as a function of the field [black and red circles in Fig. 3(c)] and the field dependence of T_1 and T_2 peaks in the C_m data [Fig. 3(e)]. There are five phases in the phase diagram [Fig. 3(e)]. Phase 1 is the closest region to the zero-field ground state investigated by neutron diffraction (Fig. 2). Its horizontal and vertical boundaries correspond, respectively, to the

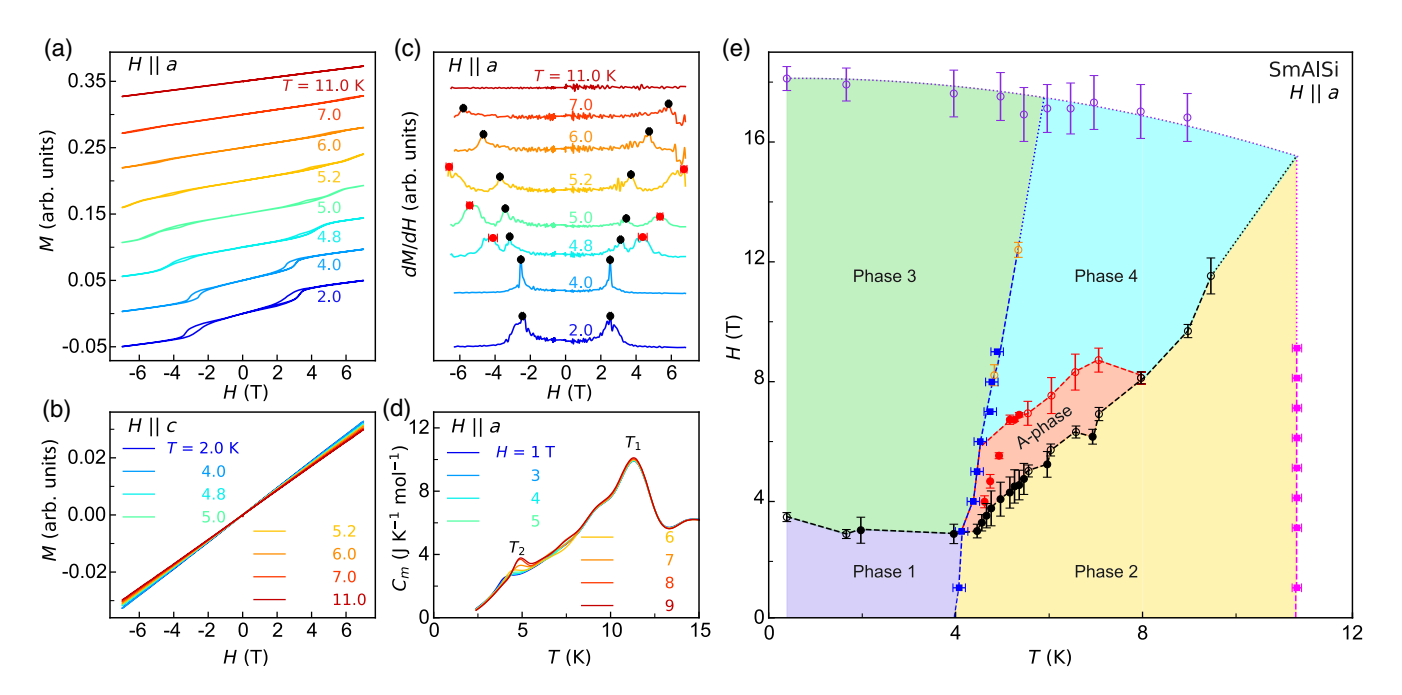


FIG. 3. (a) Magnetization curves with $H\|a$ at several temperatures. The 2 K curve has correct values in units of μ_B , and the rest of the curves are shifted uniformly to improve visibility. (b) M(H) curves with $H\|c$ are strictly linear. (c) Derivatives of the $M(H\|a)$ curves reveal two sets of peaks (black and red circles) that define the A-phase boundaries. (d) Magnetic heat capacity as a function of temperature $C_m(T)$ at several fields with $H\|a$. (e) The phase diagram of SmAlSi. The filled magenta and blue squares correspond to T_1 and T_2 , respectively. The filled black and red circles are from (c). All empty symbols are from the high-field data in Fig. S3 [24].

black peaks in dM/dH and T_2 peaks in the C_m data [Figs. 3(c) and 3(d)]. Phase 2 is bound vertically by the T_1 and T_2 peaks in the C_m data [Fig. 3(d)]. It is bound horizontally by the black peaks in dM/dH [filled black circles in Figs. 3(c) and 3(e)] and hysteresis loops in the high-field magnetic torque data [empty black circles in Fig. 3(e)]. The high-field data are shown in Supplemental Material [24] (Fig. S3). Phase 3 is horizontally bound by the black peaks in dM/dH and purple circles representing the saturation of the high-field torque signal (Fig. S3). It is vertically bound by the T_2 peaks in the C_m data [blue squares in Fig. 3(e)] and steps in the high-field torque data (open orange circles) [24]. The two sets of dM/dHpeaks [black and red symbols in Figs. 3(c) and 3(e)] encompass a red phase in the middle. In the discussion below, the observation of THE indicates that this phase is likely to be an A phase, similar to the A phase in materials such as GaV₄(S, Se)₈ and Gd₂PdSi₃ where skyrmions are found [28–31]. Phase 4 is separated from the A phase by the red dM/dH peaks in Fig. 3(c) and hysteresis loops in the high-field torque data [open red circles in Figs. 3(e) and S3]. More details about the angle dependence of the phase diagram are provided in Figs. S4 and S5 [24].

D. Hall effect

Confirming skyrmions in the A phase of SmAlSi is challenging given the lack of isotope-rich samples for small angle neutron scattering (SANS). However, we detect a topological (magnetically driven) Hall signal ρ_{xy}^T which largely overlaps with the temperature and field range of the A phase, which indicates a nonzero average spin chirality as observed in skyrmion lattices [31,32]. Figure 4(a) shows the total Hall signal $\rho_{xy} = \rho_{xy}^O + \rho_{xy}^T$ measured with the field directed at different angles (θ) with respect to the caxis in the ac plane, as indicated in the inset. There are no hysteretic patterns in the Hall effect; i.e., the conventional anomalous Hall effect (AHE) $\rho_{xy}^A \propto M(H)$ is indiscernible in our data. In fact, a conventional AHE is not expected in SmAlSi with purely AFM order. The underlying nonlinear field dependence of the ordinary Hall signal $\rho_{xy}^{O}(H)$ results from multiband conduction [33], which is fitted to a threeband model [dashed lines in Fig. 4(a)]. Details of the threeband model are discussed in Supplemental Material [24] (Fig. S6). The topological Hall signal $\rho_{xy}^T = \rho_{xy} - \rho_{xy}^O$ is highlighted with colors in Fig. 4(a). Note that ρ_{xy}^T is observed at T = 5 K between 4 and 7 T, which is approximately the same region where the A phase is observed. Using a similar analysis, we also isolate the ρ_{xy}^T signal with the field in the ab plane, and those data are shown in Fig. 4(b).

The dependence of ρ_{xy}^T on the magnetic field direction provides information about the nature of the DM interaction. The only source of anisotropy for the Hall effect in the ab plane is the existence of a preferred plane for the spin vectors shaped by the DM interaction (see

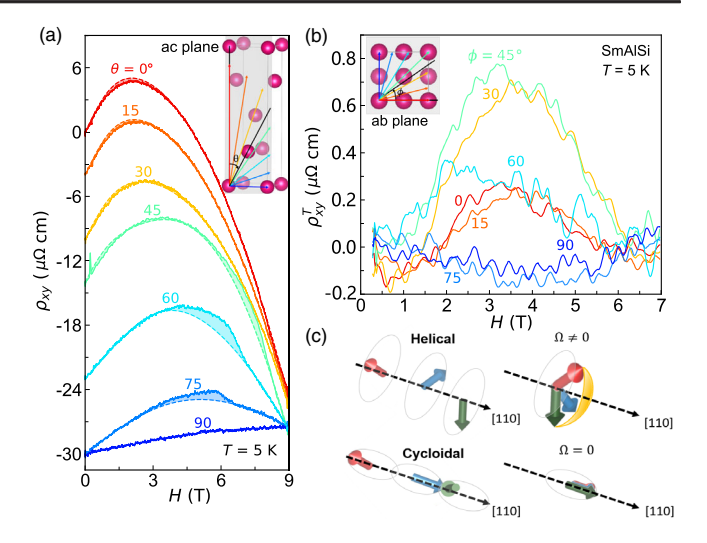


FIG. 4. (a) The Hall data $\rho_{xy}(H)$ are shown at 5 K with the field pointing at several angles in the ac plane as indicated in the inset. (b) Topological Hall signal $\rho_{xy}^T(H)$ is shown at 5 K with several field angles in the ab plane. (c) The solid angle $\Omega = \mathbf{S}_1 \cdot (\mathbf{S}_2 \times \mathbf{S}_3)$ made by three spins is maximized when the field is along the spiral propagation direction in a helical order. It is minimized in a cycloidal order.

Supplemental Material [24] for a detailed explanation). The magnetic field is most effective in canting the spins and enhancing their chirality when it is perpendicular to this preferred plane [see Fig. 4(c)]. Our measurements of the THE in the ab plane, presented in Fig. 4(b), show that ρ_{xy}^T is maximized when the field points at $\phi = 45^{\circ}$ with respect to the a axis, i.e., parallel to the spiral's propagation direction [110]. This observation excludes the possibility of a purely cycloidal order [Fig. 4(c)] which is expected from the conventional DM interaction; instead, it indicates a helical or a mixed spiral state with a dominant helical component, as expected from Weyl-induced DM interactions. Theoretically, the **D** vector must be parallel (perpendicular) to the spin-spin links if the Weyl-induced (conventional) DM interaction is dominant, favoring a helical (cycloidal) order [8,9]. For THE measured in the ac plane, the maximum ρ_{xy}^T is reached when the field points at the angle $\theta = 60^{\circ}$ with respect to the c axis, and it vanishes when the field is directed along the a axis ($\theta = 90^{\circ}$). This also requires a sizable helical component within a generally mixed spiral order. Note that the Hall signal becomes nearly featureless at $\theta = 90^{\circ}$ due to the geometry of this measurement (see the inset in Fig. S6 [24]).

Importantly, the size of ρ_{xy}^T in the A phase of SmAlSi reaches a maximum of 0.8 $\mu\Omega$ cm in the ab plane and 1.7 $\mu\Omega$ cm in the ac plane (Figs. 4 and S6), comparable to the giant topological Hall effect in the skyrmion system Gd_2PdSi_3 and one order of magnitude larger than in FeGe [31,32]. The ρ_{xy}^T signal is lost at temperatures lower or higher than the A-phase boundaries. Such a large THE confined to the boundaries of the A phase is considered a

hallmark of topological magnetic textures such as skyrmions [31,32].

E. Electronic structure

The observation of a spiral magnetic ground state, a large THE, and an A phase in SmAlSi indicates sizable DM and chiral interactions. Recent calculations show that Weyl electrons could mediate such interactions by coupling to the local f moments through an RKKY mechanism [8–11]. The band structure of SmAlSi in Fig. 5(a) has the necessary ingredients for Weyl-mediated RKKY interactions, namely, (i) localized f bands well below the Fermi level (E_F) , (ii) a small density of states (DOS) near E_F from the linearly dispersing bands with Weyl crossings, and (iii) intraband k-space vectors (nesting vectors) that match the magnetic ordering vectors and link topologically nontrivial Fermi pockets. To verify the last point, we visualize the Fermi surface of SmAlSi from DFT + SOC + U calculations in the field-driven FM state. It comprises small hole and electron pockets [Figs. 5(b) and 5(c)] and 20 pairs of Weyl

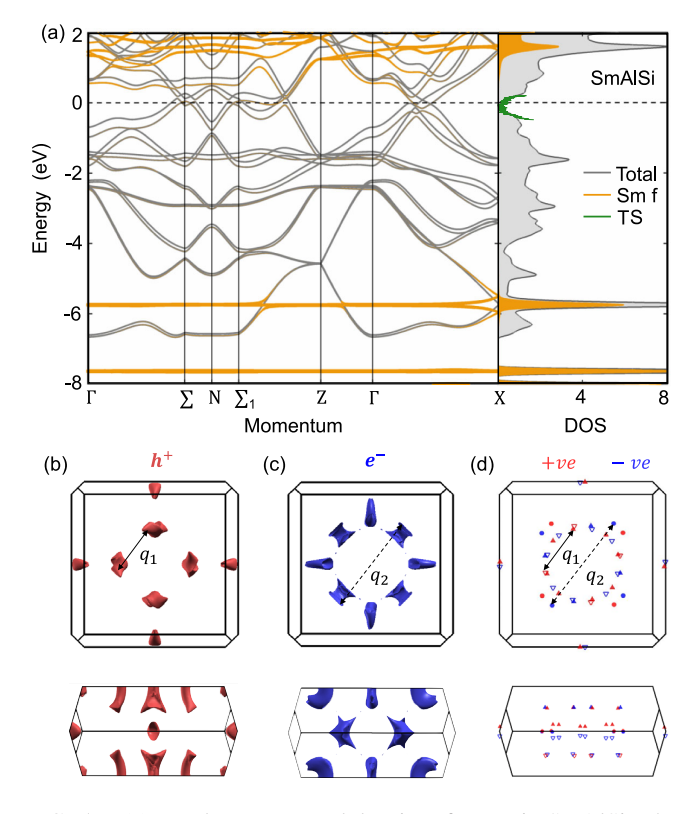


FIG. 5. (a) Band structure and density of states in SmAlSi. The Fermi energy E_F is marked by a dashed line, and the f bands are highlighted in orange. The green curve in the DOS panel on the right is obtained experimentally by tunneling spectroscopy (TS) and confirms that the DOS near E_F is due to Weyl electrons by revealing its quadratic energy dependence. (b) Top and side views of the hole pocket in the first BZ. (c) The same views of the electron pocket. (d) A map of the Weyl nodes where the circles, full triangles, and empty triangles represent Weyl nodes at $k_z = 0$, $k_z > 0$, and $k_z < 0$, respectively.

nodes [Fig. 5(d)] in the first Brillouin zone (1BZ). Details of the DFT calculations are presented in Supplemental Material [24], where the Weyl nodes are categorized into five groups (W_1 – W_5) based on their symmetries and energies (Figs. S7 and S8). The closest and farthest Weyl nodes with respect to E_F are W_1 and W_3 nodes at E=0 and 89 meV, respectively (Fig. S8).

As shown in Figs. 5(b) and 5(c), two momentum space vectors $\mathbf{q_1} = (\frac{1}{3} - \delta, \frac{1}{3} - \delta, 0)$ and $\mathbf{q_2} = (\frac{2}{3} + \delta, \frac{2}{3} + \delta, 0)$ connect topologically nontrivial Fermi pockets. Both nesting vectors are consistent with the observed spiral ordering vector $\mathbf{k} = (\frac{1}{3} - \delta, \frac{1}{3} - \delta, 0)$ in Fig. 2. We confirm the accuracy of our DFT calculations by comparing the theoretical dimensions of the Fermi pockets to the frequency of the quantum oscillations in Fig. S9 [24,34]. We also confirm the accuracy of our DOS calculation near E_F by comparing it to scanning tunneling spectroscopic data in Fig. 5(a). Since the conventional RKKY coupling is propositional to DOS, it must be small in SmAlSi due to a small DOS at E_F . However, the Weyl-mediated RKKY interactions can be strong even in the absence of a Fermi sea due to the Weyl DOS that grows quadratically with energy and makes the high-energy Weyl states most influential in the dynamics of local moments [9].

Although similar nesting conditions between the Weyl nodes can be found in the band structures of CeAlSi, PrAlSi, and NdAlSi (Fig. S7) [15,27,35], the strong MCA blocks spiral ordering in those systems. PrAlSi has an outof-plane FM order, while CeAlSi has an in-plane noncollinear FM order, and neither one shows evidence of DM interactions [27]. NdAlSi has an incommensurate AFM order at intermediate temperatures whose ordering vectors match the q_1 and q_2 nesting vectors [15]. The magnetic Bragg peaks associated with the q_1 and q_2 vectors are, respectively, refined to a small in-plane helical spin component and a large out-of-plane Ising component with a net FM moment. The Ising character of the NdAlSi incommensurate order caused by a strong MCA dominates the Weyl-mediated RKKY interaction, and, upon cooling, a commensurate ferrimagnetic ground state is ultimately reached. For SmAlSi, however, our observation of a quasi-isotropic magnetocrystalline interaction and the complete absence of ferromagnetism suggest that an AFM spiral order could be stabilized by Weyl-mediated RKKY interactions. An interesting related material is CeAlGe that shows evidence of meron excitations in SANS measurements [36].

F. Monte Carlo simulations

Our band structure calculation in Fig. 5 indicates that the Fermi pockets mostly comprise Weyl electrons in SmAlSi. Multiple pairs of same-chirality Weyl nodes are separated in the 1BZ by nearly commensurate wave vectors \mathbf{q}_1 and \mathbf{q}_2 . Theoretically [9], such Weyl nodes promote precisely the type of magnetic order seen in the experiment.

The RKKY spin interactions induced by Weyl electrons [9] include Heisenberg (H), Dzyaloshinskii-Moriya (DM), and Kitaev-Ising (I) interactions:

$$H = \sum_{ij} [J_{ij} \mathbf{S}_i \cdot \mathbf{S}_j + \mathbf{D}_{ij} \cdot (\mathbf{S}_i \times \mathbf{S}_j) + I_{ij} (\mathbf{S}_i \cdot \hat{\mathbf{n}}_{ij}) (\mathbf{S}_j \cdot \hat{\mathbf{n}}_{ij})].$$
(1)

Every pair of Weyl nodes imparts a "mode" of signchanging spatial oscillations on these couplings, characterized by the node-separation wave vector \mathbf{q} . In response to the oscillation modes at many wave vectors \mathbf{q} , a stable magnetic order with minimal unit cell takes advantage of the largest nearly commensurate wave vectors available, i.e., $\mathbf{q} \in {\mathbf{q}_1, \mathbf{q}_2}$ in SmAlSi. The absence of large conventional Fermi pockets, as well as the striking correlation between the observed magnetic ordering wave vectors and the locations of Weyl nodes in the 1BZ, is the first indication that the Weyl-induced RKKY interactions are responsible for the magnetism of SmAlSi. Any intrinsic RKKY interaction due to conventional itinerant electrons is weak due to a small DOS at E_F . Also, the superexchange interactions among the localized f electrons are weak, as shown in Supplemental Material [24].

The Heisenberg interaction [first term in Eq. (1)] induced by a single pair of Weyl nodes stabilizes by itself a spiral magnetic order at the internode wave vector \mathbf{q} , but all types of helical, cycloidal, and mixed spirals are equally likely. Once a spiral is established, the DM interaction [second term in Eq. (1)] determines its type. If the Weyl spectrum is spherically symmetric, $\epsilon_{\bf k}=\pm v|{\bf k}|,$ then the **D** vectors of the induced DM interaction are parallel to the extendedrange links between the two interacting spins. This promotes the helical spiral state [24], because the spins prefer to be perpendicular to **D**. Generic tilted type-I Weyl nodes with spectrum $\epsilon_{\mathbf{k}} = \pm v|\mathbf{k}| - \mathbf{u} \cdot \mathbf{k}$ may push **D** away from the link direction in proportion to the amount of tilt $|\mathbf{u}|$, resulting in a mixed spiral with a cycloidal component. Note that the conventional intrinsic mechanism normally yields a different **D** vector which is perpendicular to the nearest-bond directions in the ab planes and selects a pure cycloidal spiral [24]. The Kitaev-Ising interaction [third term in Eq. (1)] is found to be less important [24].

We use Monte Carlo simulations to produce a theoretical phase diagram of the model Hamiltonian in Eq. (1) and analyze its spin anisotropy (Fig. 6). The technical details of Monte Carlo simulations are presented in Supplemental Material (Figs. S10–S12) [24]. The phase diagram is explored at zero magnetic field and consists of one or two magnetically ordered low-temperature phases [Figs. 6(a) and 6(b)] and the disordered high-temperature phase [Fig. 6(d)]. This qualitatively mirrors the two experimentally observed phase transitions at zero field in SmAlSi (T_1 and T_2 in Fig. 1). The low-temperature phase ($T < T_1$) is the spin spiral. The intermediate state ($T_1 < T < T_2$) has

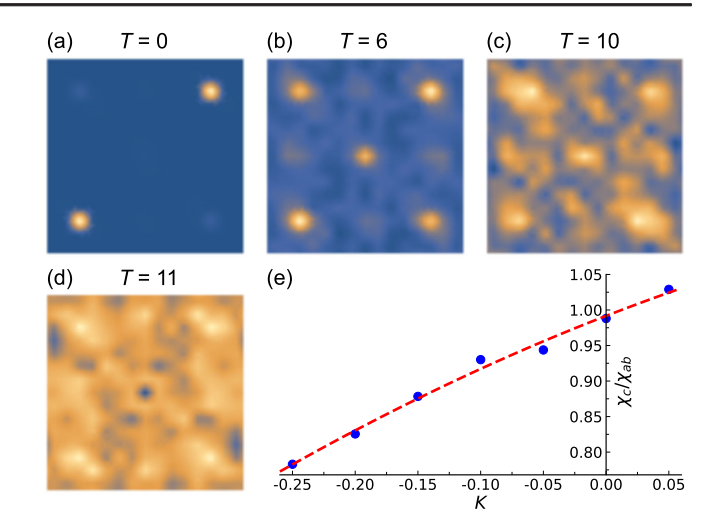


FIG. 6. The Monte Carlo spin dynamics in zero magnetic field, without interlayer, DM, and Kitaev-Ising interactions. (a)–(d) The Fourier transform of a magnetization component is integrated over k_c and shown as a function of (k_a, k_b) . There is a phase transition between a low-temperature spiral and another possibly ordered state at $T \sim 5$. Magnetic order is surely lost above $T \sim 10$. (e) Magnetic susceptibility ratio χ_c/χ_{ab} of the low-temperature spiral state as a function of the anisotropy coupling K. The red curve is a guide to the eye. All model parameters, including T, are expressed in the same arbitrary units.

a more complicated structure in the Monte Carlo, which requires further theoretical study with finite-size scaling and exploration in a broad parameter space. In the absence of isotope-rich samples, our neutron diffraction data cannot resolve all details of the magnetic structure at temperatures between T_1 and T_2 .

The spin anisotropy $K(S_c)^2$ in the simulated classical model Hamiltonian [Fig. 6(e)] is found to have little effect on the spin dynamics even when the corresponding susceptibility ratio reaches the value $\chi_c/\chi_a \approx 0.8$ at T=0 seen in SmAlSi. In other words, the microscopic anisotropy leading to $\chi_c/\chi_a \approx 0.8$ at T=0 leaves the spins almost undisturbed in their fluctuations governed by the induced RKKY interactions. Larger amounts of anisotropy eventually lead to either the easy-axis or easy-plane orders. The former is found in NdAlSi, while the latter still admits cycloidal spirals and is likely relevant to CeAlGe [36].

IV. CONCLUSION

Recent theoretical works predict that chiral Weyl fermions can induce a spiral magnetic order by coupling to the local moments via an RKKY interaction. Evidence of such interactions is reported in NdAlSi, but a spiral order is not found due to strong Ising anisotropy that prevents spins from rotating. The key insight in this work is to recognize that establishing a spiral order needs nearly isotropic spins, i.e., a small MCA, in addition to nesting between the Weyl nodes. Both conditions are satisfied in SmAlSi.

We make a compelling case for Weyl-induced magnetism in SmAlSi as follows. (i) Using neutron scattering, we find a spiral order with a periodicity that is linked to the distance in momentum space between the Weyl nodes. (ii) We find an A phase in the magnetic phase diagram of SmAlSi using magnetization, heat capacity, and highfield magnetic torque measurements. (iii) Within the boundaries of the A phase, we observe a large THE with the magnitude of 1–2 $\mu\Omega\,cm,$ comparable to giant THE in skyrmion materials. (iv) The angle dependence of THE with the field in both ab and ac planes is consistent with a dominant helical component in the spiral order. This is important evidence for Weyl-mediated RKKY interactions, since the conventional DM interaction imposes a strictly cycloidal order in the tetragonal structure of SmAlSi. (v) Monte Carlo simulations based on the theoretical model of Weyl-induced RKKY interactions confirm the experimentally observed spiral order in SmAlSi and provide supporting evidence for its helical character, nearly isotropic dynamics, and phase boundary in zero field. More work is necessary to understand the microscopic details of the complex spiral order of SmAlSi using probes such as NMR, µSR, and resonant inelastic x-ray scattering.

We end by mentioning three implications of our results. First, the Weyl-induced RKKY interaction is a new mechanism for stabilizing spiral order and skyrmions that are in demand for high-density and high-speed magnetic memories. Second, the competition between Weyl-induced and conventional RKKY interactions in topological semimetals could be used to tune cycloidal versus helical spin textures. Finally, Weyl dispersion can be anisotropic in real lattices, and the degree of this anisotropy can also be used to tune the helical versus cycloidal components.

ACKNOWLEDGMENTS

F. T. and P. N. thank I. Mazin for helpful discussions. This material is based upon work supported by the Air Force Office of Scientific Research (AFOSR) under Grant No. FA2386-21-1-4059. The authors thank D. Haskel, P. Ryan, L. Rijos-Carretero, W. Koll, and J. A. Gupta for helpful discussions. S.-M. H. is supported by the MOST-AFOSR Taiwan program on Topological and Nanostructured Materials, Grant No. 110-2124-M-110-002-MY3. A portion of this research used resources at the High Flux Isotope Reactor, a DOE Office of Science User Facility operated by Oak Ridge National Laboratory. Any mention of commercial products is intended solely for fully detailing experiments; it does not imply recommendation or endorsement by NIST. A portion of this work was performed at the National High Magnetic Field Laboratory, which is supported by the National Science Foundation Cooperative Agreement No. DMR-1644779 and the state of Florida. P. N. acknowledges support from the Institute for Quantum Matter, an Energy Frontier Research Center funded by the U.S. Department of Energy, Office of Science, Basic Energy Sciences under Grant No. DE-SC0019331. The work at Northeastern University was supported by the U.S. Department of Energy (DOE), Office of Science, Basic Energy Sciences Grant No. DE-SC0022216 and benefited from Northeastern University's Advanced Scientific Computation Center and the Discovery Cluster and the National Energy Research Scientific Computing Center through DOE Grant No. DE-AC02-05CH11231. The work at TIFR Mumbai was supported by the Department of Atomic Energy of the Government of India under Project No. 12-R&D-TFR-5.10-0100. The work at Temple University was funded by the National Science Foundation under Grant No. NSF/DMR-1945222. R. Z. and J. S. acknowledge the support of the U.S. Office of Naval Research (ONR) Grant No. N00014-22-1-2673.

- [1] Y. Tokura, K. Yasuda, and A. Tsukazaki, *Magnetic Topological Insulators*, Nat. Rev. Phys. 1, 126 (2019).
- [2] Z.-C. Wang, J. D. Rogers, X. Yao, R. Nichols, K. Atay, B. Xu, J. Franklin, I. Sochnikov, P. J. Ryan, D. Haskel, and F. Tafti, *Colossal Magnetoresistance without Mixed Valence in a Layered Phosphide Crystal*, Adv. Mater. 33, 2005755 (2021).
- [3] A. J. Bestwick, E. J. Fox, X. Kou, L. Pan, K. L. Wang, and D. Goldhaber-Gordon, *Precise Quantization of the Anomalous Hall Effect near Zero Magnetic Field*, Phys. Rev. Lett. 114, 187201 (2015).
- [4] C. Hu, L. Ding, K. N. Gordon, B. Ghosh, H.-J. Tien, H. Li, A. G. Linn, S.-W. Lien, C.-Y. Huang, S. Mackey, J. Liu, P. V. S. Reddy, B. Singh, A. Agarwal, A. Bansil, M. Song, D. Li, S.-Y. Xu, H. Lin, H. Cao, T.-R. Chang, D. Dessau, and N. Ni, *Realization of an Intrinsic Ferromagnetic Topological State in* MnBi₈Te₁₃, Sci. Adv. 6, eaba4275 (2020).
- [5] C. Liu, Y. Wang, H. Li, Y. Wu, Y. Li, J. Li, K. He, Y. Xu, J. Zhang, and Y. Wang, Robust Axion Insulator and Chern Insulator Phases in a Two-Dimensional Antiferromagnetic Topological Insulator, Nat. Mater. 19, 522 (2020).
- [6] Y. Sun, C. Lee, H.-Y. Yang, D. H. Torchinsky, F. Tafti, and J. Orenstein, *Mapping Domain-Wall Topology in the Magnetic Weyl Semimetal* CeAlSi, Phys. Rev. B 104, 235119 (2021).
- [7] B. Xu, J. Franklin, A. Jayacody, H.-Y. Yang, F. Tafti, and I. Sochnikov, Back Cover: Picoscale Magnetoelasticity Governs Heterogeneous Magnetic Domains in a Noncentrosymmetric Ferromagnetic Weyl Semimetal, Adv. Quantum Technol. 4, 2170033 (2021).
- [8] P. Nikolić, *Universal Spin Wave Damping in Magnetic Weyl Semimetals*, Phys. Rev. B **104**, 024414 (2021).
- [9] P. Nikolić, Dynamics of Local Magnetic Moments Induced by Itinerant Weyl Electrons, Phys. Rev. B 103, 155151 (2021).
- [10] S.-X. Wang, H.-R. Chang, and J. Zhou, RKKY Interaction in Three-Dimensional Electron Gases with Linear Spin-Orbit Coupling, Phys. Rev. B 96, 115204 (2017).

- [11] H.-R. Chang, J. Zhou, S.-X. Wang, W.-Y. Shan, and D. Xiao, RKKY Interaction of Magnetic Impurities in Dirac and Weyl Semimetals, Phys. Rev. B 92, 241103(R) (2015).
- [12] Z. Wang, Y. Su, S.-Z. Lin, and C. D. Batista, Meron, Skyrmion, and Vortex Crystals in Centrosymmetric Tetragonal Magnets, Phys. Rev. B 103, 104408 (2021).
- [13] J. Repicky, P.-K. Wu, T. Liu, J. P. Corbett, T. Zhu, S. Cheng, A. S. Ahmed, N. Takeuchi, J. Guerrero-Sanchez, M. Randeria, R. K. Kawakami, and J. A. Gupta, *Atomic-Scale Visualization of Topological Spin Textures in the Chiral Magnet* MnGe, Science 374, 1484 (2021).
- [14] S. Luo and L. You, Skyrmion Devices for Memory and Logic Applications, APL Mater. 9, 050901 (2021).
- [15] J. Gaudet, H.-Y. Yang, S. Baidya, B. Lu, G. Xu, Y. Zhao, J. A. Rodriguez-Rivera, C. M. Hoffmann, D. E. Graf, D. H. Torchinsky, P. Nikolić, D. Vanderbilt, F. Tafti, and C. L. Broholm, Weyl-Mediated Helical Magnetism in NdAlSi, Nat. Mater. 20, 1650 (2021).
- [16] A. Neubauer, C. Pfleiderer, B. Binz, A. Rosch, R. Ritz, P. G. Niklowitz, and P. Böni, *Topological Hall Effect in the A Phase of MnSi*, Phys. Rev. Lett. 102, 186602 (2009).
- [17] M. Hirschberger, T. Nakajima, S. Gao, L. Peng, A. Kikkawa, T. Kurumaji, M. Kriener, Y. Yamasaki, H. Sagayama, H. Nakao, K. Ohishi, K. Kakurai, Y. Taguchi, X. Yu, T.-h. Arima, and Y. Tokura, Skyrmion Phase and Competing Magnetic Orders on a Breathing Kagomé Lattice, Nat. Commun. 10, 5831 (2019).
- [18] L. Xu, H. Niu, Y. Bai, H. Zhu, S. Yuan, X. He, Y. Yang, Z. Xia, L. Zhao, and Z. Tian, Shubnikov-de Haas Oscillations and Nontrivial Topological State in Weyl Semimetal Candidate SmAlSi, J. Phys. Condens. Matter 34, 485701 (2022).
- [19] J. Rodríguez-Carvajal, Recent Advances in Magnetic Structure Determination by Neutron Powder Diffraction, Physica (Amsterdam) 192B, 55 (1993).
- [20] A. Wills, A New Protocol for the Determination of Magnetic Structures Using Simulated Annealing and Representational Analysis (Sarah), Physica (Amsterdam) 276B–278B, 680 (2000).
- [21] P. Blaha, K. Schwarz, F. Tran, R. Laskowski, G. K. H. Madsen, and L. D. Marks, WIEN2K: An APW + lo Program for Calculating the Properties of Solids, J. Chem. Phys. 152, 074101 (2020).
- [22] J. P. Perdew, K. Burke, and M. Ernzerhof, Generalized Gradient Approximation Made Simple, Phys. Rev. Lett. 77, 3865 (1996).
- [23] V. I. Anisimov, J. Zaanen, and O. K. Andersen, *Band Theory and Mott Insulators: Hubbard U instead of Stoner I*, Phys. Rev. B **44**, 943 (1991).
- [24] See Supplemental Material at http://link.aps.org/ supplemental/10.1103/PhysRevX.13.011035 for detailed information about the crystal structure, experimental methods, phase diagram, and theoretical calculations.
- [25] M. Lyu, J. Xiang, Z. Mi, H. Zhao, Z. Wang, E. Liu, G. Chen, Z. Ren, G. Li, and P. Sun, *Nonsaturating Magnetoresist*-

- ance, Anomalous Hall Effect, and Magnetic Quantum Oscillations in the Ferromagnetic Semimetal PrAlSi, Phys. Rev. B **102**, 085143 (2020).
- [26] G. Chang, B. Singh, S.-Y. Xu, G. Bian, S.-M. Huang, C.-H. Hsu, I. Belopolski, N. Alidoust, D. S. Sanchez, H. Zheng, H. Lu, X. Zhang, Y. Bian, T.-R. Chang, H.-T. Jeng, A. Bansil, H. Hsu, S. Jia, T. Neupert, H. Lin, and M. Z. Hasan, Magnetic and Noncentrosymmetric Weyl Fermion Semimetals in the RAIGe Family of Compounds (R = rare earth), Phys. Rev. B 97, 041104(R) (2018).
- [27] H.-Y. Yang, B. Singh, J. Gaudet, B. Lu, C.-Y. Huang, W.-C. Chiu, S.-M. Huang, B. Wang, F. Bahrami, B. Xu, J. Franklin, I. Sochnikov, D. E. Graf, G. Xu, Y. Zhao, C. M. Hoffman, H. Lin, D. H. Torchinsky, C. L. Broholm, A. Bansil, and F. Tafti, Noncollinear Ferromagnetic Weyl Semimetal with Anisotropic Anomalous Hall Effect, Phys. Rev. B 103, 115143 (2021).
- [28] E. Ruff, S. Widmann, P. Lunkenheimer, V. Tsurkan, S. Bordács, I. Kézsmárki, and A. Loidl, *Multiferroicity* and Skyrmions Carrying Electric Polarization in GaV₄S₈, Sci. Adv. 1, e1500916 (2015).
- [29] Y. Fujima, N. Abe, Y. Tokunaga, and T. Arima, Thermodynamically Stable Skyrmion Lattice at Low Temperatures in a Bulk Crystal of Lacunar Spinel GaV₄Se₈, Phys. Rev. B 95, 180410(R) (2017).
- [30] S. Bordács, A. Butykai, B. G. Szigeti, J. S. White, R. Cubitt, A. O. Leonov, S. Widmann, D. Ehlers, H.-A. K. von Nidda, V. Tsurkan, A. Loidl, and I. Kézsmárki, *Equilibrium Skyrmion Lattice Ground State in a Polar Easy-Plane Magnet*, Sci. Rep. 7, 7584 (2017).
- [31] T. Kurumaji, T. Nakajima, M. Hirschberger, A. Kikkawa, Y. Yamasaki, H. Sagayama, H. Nakao, Y. Taguchi, T.-h. Arima, and Y. Tokura, Skyrmion Lattice with a Giant Topological Hall Effect in a Frustrated Triangular-Lattice Magnet, Science 365, 914 (2019).
- [32] M. Leroux, M. J. Stolt, S. Jin, D. V. Pete, C. Reichhardt, and B. Maiorov, *Skyrmion Lattice Topological Hall Effect near Room Temperature*, Sci. Rep. **8**, 15510 (2018).
- [33] H. Lin, Y. Li, Q. Deng, J. Xing, J. Liu, X. Zhu, H. Yang, and H.-H. Wen, Multiband Superconductivity, *Large Anisotropy in FeS Crystals*, Phys. Rev. B 93, 144505 (2016).
- [34] P. M. C. Rourke and S. R. Julian, Numerical Extraction of de Haas-van Alphen Frequencies from Calculated Band Energies, Comput. Phys. Commun. 183, 324 (2012).
- [35] H.-Y. Yang, B. Singh, B. Lu, C.-Y. Huang, F. Bahrami, W.-C. Chiu, D. Graf, S.-M. Huang, B. Wang, H. Lin, D. Torchinsky, A. Bansil, and F. Tafti, *Transition from Intrinsic* to Extrinsic Anomalous Hall Effect in the Ferromagnetic Weyl Semimetal PrAlGe_{1-x}Si_x, APL Mater. 8, 011111 (2020).
- [36] P. Puphal, V. Pomjakushin, N. Kanazawa, V. Ukleev, D. J. Gawryluk, J. Ma, M. Naamneh, N. C. Plumb, L. Keller, R. Cubitt, E. Pomjakushina, and J. S. White, *Topological Magnetic Phase in the Candidate Weyl Semimetal CeAlGe*, Phys. Rev. Lett. **124**, 017202 (2020).